Quantifying the role of different surface coatings in experimental models of wound healing

Wang Jin [a,*], Kai-Yin Lo [b], Yung-Shin Sun [c], Ya-Han Ting [b], Matthew J Simpson [a],

[a] *School of Mathematical Sciences, Queensland University of Technology (QUT) Brisbane, Queensland 4000, Australia.*

[b] *Department of Agricultural Chemistry, National Taiwan University Taipei 10617, Taiwan.*

[c] *Department of Physics, Fu-Jen Catholic University, Taipei 242, Taiwan.*

Abstract

In vitro surface coatings are widely used to mimic the role of extracellular matrix in the *in vivo* environment. Different surface coatings lead to different effects, with some studies showing inconsistent results. To explore the role of different surface coatings, we use a newly developed wound-healing assay, called a *stopper assay*, with two commonly used surface coatings: gelatin and poly-L-lysine (PLL). Our experimental data show the wound width decreases faster with the gelatin and PLL coatings. Similarly, the number of cells in certain subregions increases faster with these coatings. Unfortunately, neither of these observations provides definitive mechanistic insight into the role of the coatings. To provide such insight we calibrate the solution of the Fisher-Kolmogorov model to match the experimental data. Our parameter estimates indicate that both coatings significantly increase cell motility without affecting cell proliferation.

Key words: Wound healing assay; Stopper assay; Surface coating; Fisher-Kolmogorov; Reaction-diffusion; Transport

1 Introduction

In vitro surface coatings are used as a fundamental experimental approach to mimic and study the effect of the extracellular matrix (ECM) in the *in vivo* environment. It is important to include effects of the ECM in experimental studies because the ECM interacts with cells both physically and chemically, and affects cell behaviour, tissue development, and cancer progression (Hay 2013; Horiguchi et al., 2012; Screen et al., 2015; Vedula et al., 2013). Popular choices of coating reagents include gelatin, poly-L-lysine (PLL), collagen, and fibronectin (Liberio et al., 2014; McCarthy et al., 1983; McIntosh et al., 1988). In the literature, gelatin is thought to increase both cell motility and proliferation (McCarthy et al., 1983; McIntosh et al., 1988), while PLL can have the opposite effects (Liberio et al., 2014). In contrast, other studies suggest that PLL may have no impact on cell motility or proliferation (Fischer et al., 2007; Rangappa et al., 2000). Since these observations are inconsistent, the precise role of surface coatings remains unclear.

Among various types of *in vitro* experiments, wound-healing assays are widely used to study cell motility and cell proliferation under different conditions, including different surface coatings (Ascione et al., 2017; Liberio et al., 2014; Tremel et al., 2009). Wound-healing assays can be used to provide quantitative insight by measuring rates of wound closure or measuring the increase in the numbers of cells in particular subregions of the experiment (Johnston et al., 2014; Liberio et al., 2014; McCarthy et al., 1983; Treloar and Simpson, 2013). However, neither of these measurements can tease apart the intricate interplay between the effects of cell migration and cell proliferation that can sometimes lead to surprising results. For example, Barrandon and Green (1987) measure the temporal change in the numbers of cells in certain *in vitro* colonies and note a dramatic increase in cell numbers when TGF-α is included. This increase in cell number is due to the interplay of cell migration and cell proliferation,

* Corresponding author.
Email address: w1.jin@qut.edu.au (Wang Jin).

since TGF-α promotes migration, which then in turn provides space for the cells to proliferate (Barrandon and Green, 1987).

Mathematical models have been applied to mimic both *in vitro* and *in vivo* experiments to test biological hypotheses and to predict experimental outcomes (Jin et al., 2018a; Jove et al., 2019; Nardini et al., 2016; Sheardown and Cheng, 1996; Tam et al., 2019; Villella et al., 2019). One of the most commonly used models to study collective cell migration is the Fisher-Kolmogorov model (Fisher, 1937; Maini et al., 2004; Sherratt and Murray, 1990). The Fisher-Kolmogorov model describes the interplay between cell migration and cell proliferation by assuming cells migrate according to undirected linear diffusion and that cells proliferate logistically to a carrying capacity density. In previous studies, the Fisher-Kolmogorov model has been calibrated to match experimental data from *in vitro* wound-healing assays, and has been used to provide mechanistic insights into the role of the initial seeding density, the wound geometry, and the shape of the migration front (Jin et al., 2016; Jin et al., 2018b; Sengers et al., 2007).

In this work we apply a newly developed *in vitro* wound-healing assay, called a *stopper assay*, to explore the role of two widely used surface coatings: gelatin and PLL. One feature of the stopper assays is that cells are allowed to migrate and proliferate in the experimental well upon which only a half of the surface is coated and the other half of the surface acts as an uncoated control experiment. Our experimental data describe the wound width and the increase in the numbers of cells in particular subregions in the experiment. This data indicates that the wound closes faster, and the cell population increases faster in the gelatin- and PLL-coated regions. By calibrating the Fisher-Kolmogorov model to match the experimental data, we find that both gelatin and PLL coatings significantly increase the cell diffusivity without affecting the rate of cell proliferation.

2 Methods

2.1 Experimental methods

The stopper assays are performed in six–well experimental plates (Corning, USA), in which each experimental well has a diameter of 35 mm. Schematics of the stopper assays are illustrated in Figure 1. The lower semicircular surface of the experimental well is covered with tape (8018, 3M) to form the uncoated control area (Figure 1(a)). For the surface coating, sterile 0.1% (w/w) gelatin (Sigma, USA) or 0.1 μg/mL poly-L-lysine (Sigma, USA) prepared in 1X phosphate-buffered saline (PBS) is added to the well and incubated at 37 °C for 30 min. After the excess liquid is aspirated completely, the tape is removed, with only the upper semicircular surface of the well coated (Figure 1(a)). In the remainder of this work, we refer to the upper and lower semicircular surfaces of the experimental well as the *upper half* and the *lower half*, respectively.

We perform the experiments with the mouse embryonic fibroblast cell line NIH 3T3, purchased from the Bioresource Collection and Research Center (BCRC), Taiwan. The cell culture medium consists of Dulbecco's Modified Eagle's medium (DMEM, Gibco, USA) and 10% calf serum (CS, Invitrogen, USA). Cells are incubated in cell culture flasks (Corning, USA) under 5% CO_2 at 37 °C.

A customized I-shaped stopper (Figure 1(b)) is made of polydimethylsiloxane (PDMS, Dow Corning Sylgard$^{\text{TM}}$ 184 Silicone Elastomer, USA). The stopper is placed into the experimental well so that it is perpendicular to the boundary of the upper and lower halves (Figure 1(c)). Approximately 2.5 $\times$ 10^5 cells are seeded uniformly into the six–well experimental plates and incubated overnight (Figure 1(d)). The stopper is then removed to create a wound area (Figure 1(e)). After removing the stopper, cells are free to migrate and proliferate, eventually leading to the closure of the wound space in both the

upper and lower halves (Figure 1(g)-(i)). The wound size and the number of cells in certain subregions are measured at five equally-spaced time points: $t = 0, 12, 24, 36$, and 48 h. Each experiment is performed three times so that we can extract data from each replicate and average the data across the replicates. In this work we use data describing the each experimental replicate as well as averaged data. To distinguish these two types of the data, we use superscripts on certain variables to indicate the individual replicate number, and we use the variables with a tilde indicate averaged data.

Now that we have described the experimental protocol, we can describe some of the terminology used in the experiments. Some experiments do not involve any coating at all, and we refer to these experiments as *control* experiments. Other experiments involve applying different coatings to the experimental well. These experiments involve the upper half of the well being coated with gelatin or PLL and the lower half of the well being uncoated (Figure 1(f)). This means that we have two different types of control assays. Some of the control assays correspond to experiments where there is no coating applied to the upper half or the lower half of the well. Other control assays correspond to experiments where the upper half of the well is coated and the lower half of the well is uncoated. In Section 3.1 we plot the average data for the control experiment as well as the average data in the upper and lower halves of the wells for the experiments with gelatin and PLL coatings for the purpose of comparison. When we calibrate the solution of the Fisher-Kolmogorov model to match the experimental replicates in Section 3.3, we combine data from the two types of control assays which we refer to as the *regrouped control experiment* since both of these types of control assays do not involve any surface coating.

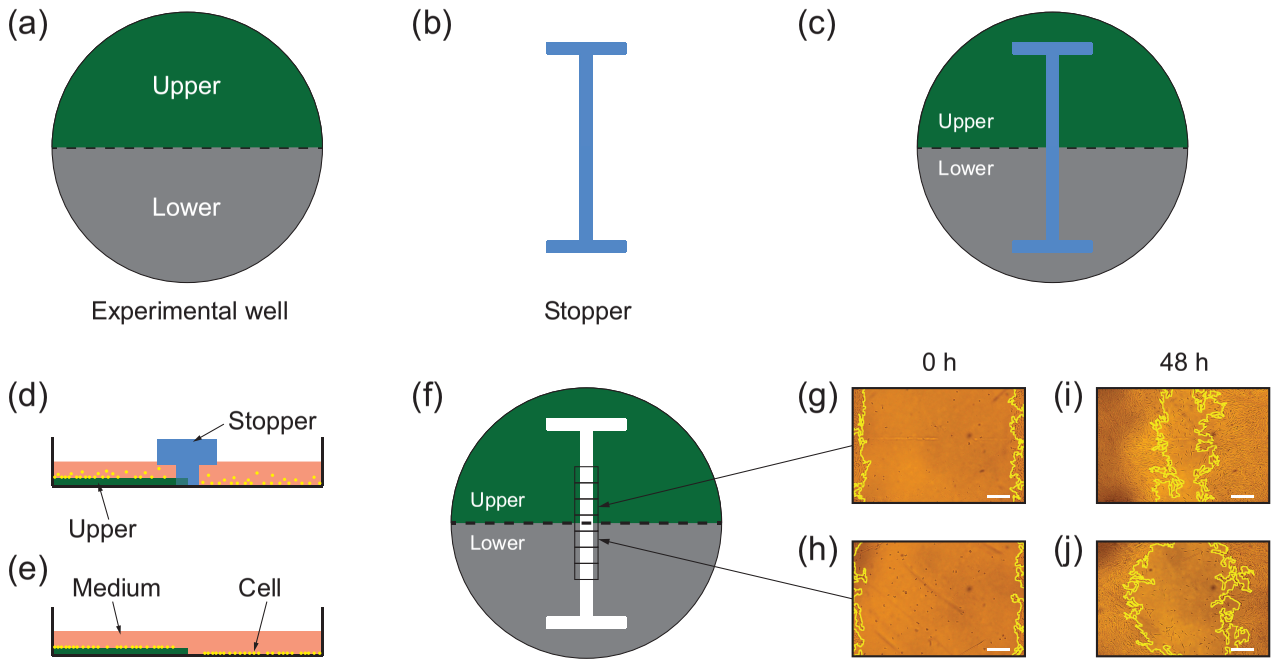

Fig. 1. **Illustrations of *in vitro* stopper assays.** (a) Experimental well in which the upper half is coated. (b) A stopper for creating the cell-free region. (c) Experimental well with a stopper placed in the middle. (d) Section of the stopper assay with a stopper in place. The thick green line indicates the upper half and the yellow dots indicate cells. (e) Section of the stopper assay after a cell monolayer is grown and the stopper is removed. (f) An illustration of how the data are retrieved from the stopper assay. The white space indicates the initial wound area. The black rectangles correspond to regions where seven experimental images are taken. (g)–(h) Experimental images taken at $t = 0$ h in the indicated upper and lower halves, shown in (f). (i)–(j) Experimental images taken at $t = 48$ h in the indicated upper and lower halves. The yellow line indicates edges of the wound area. The scale bar corresponds to 500 μm.

2.2 Edge detection and cell counting methods

We use ImageJ to detect wound edges and measure wound areas from the experimental images at $t = 0, 12, 24, 36$, and 48 h (Schindelin et al., 2015; Simpson et al., 2013). Details of the methods are described in Jin et al. (2018b). Examples of experimental images, each of which has a length of 1960 μm and a width of 1288 μm, with detected wound edges are shown in Figure 2. In the remainder of this work we refer to the area contained in the experimental image as the *experimental field-of-view*, since these images show relatively small subregions within the entire experimental well. Estimates of the wound width at each time point is calculated by taking the wound area divided by the width of the experimental field-of-view. This calculation is performed at each time point for each experimental replicate. Here we use $W^{(r)}(t)$ to represent the experimental measurement of the wound width for replicate r at time t. We then average the data to give $\widetilde{W}(t) = (1/R)\sum_{r=1}^{R} W^{(r)}(t)$, where R is the number of replicates. We report the sample mean as well as the uncertainty in our estimate by calculating the sample standard deviation.

We also manually count the number of individual cells contained in two rectangular subregions highlighted in blue in Figure 2 at $t = 0, 12, 24, 36$, and 48 h. Each subregion measures 1288 $\times$ 150 μm, and both subregions are located 300 μm away from the left and right boundaries of the experimental field-of-view, respectively. For simplicity we refer to the left-most subregion as *Subregion 1* and the right-most subregion as *Subregion 2*. These estimates are obtained at each time point for each experimental replicate. Here we use $N_1^{(r)}(t)$ and $N_2^{(r)}(t)$ to represent the experimental measurement of the number of cells within Subregion 1 and Subregion 2 for replicate r at time t, respectively. We then average the data to give $\widetilde{N_1}(t) = (1/R)\sum_{r=1}^{R} N_1^{(r)}(t)$, and $\widetilde{N_2}(t) = (1/R)\sum_{r=1}^{R} N_2^{(r)}(t)$.

Since the Subregion 1 and Subregion 2 are located symmetrically about the centre of the experimental field-of-view, we expect that the number of cells in

each subregion will be approximately equal. Therefore, we average the number of cells in the two subregions for each experimental replicate to give $N^{(r)}(t) = \left(N_1^{(r)}(t) + N_2^{(r)}(t)\right)/2$. We also average this quantity across the experimental replicates to give $\widetilde{N}(t) = \left(\widetilde{N}_1(t) + \widetilde{N}_2(t)\right)/2$. We use both of these different data types in our analysis.

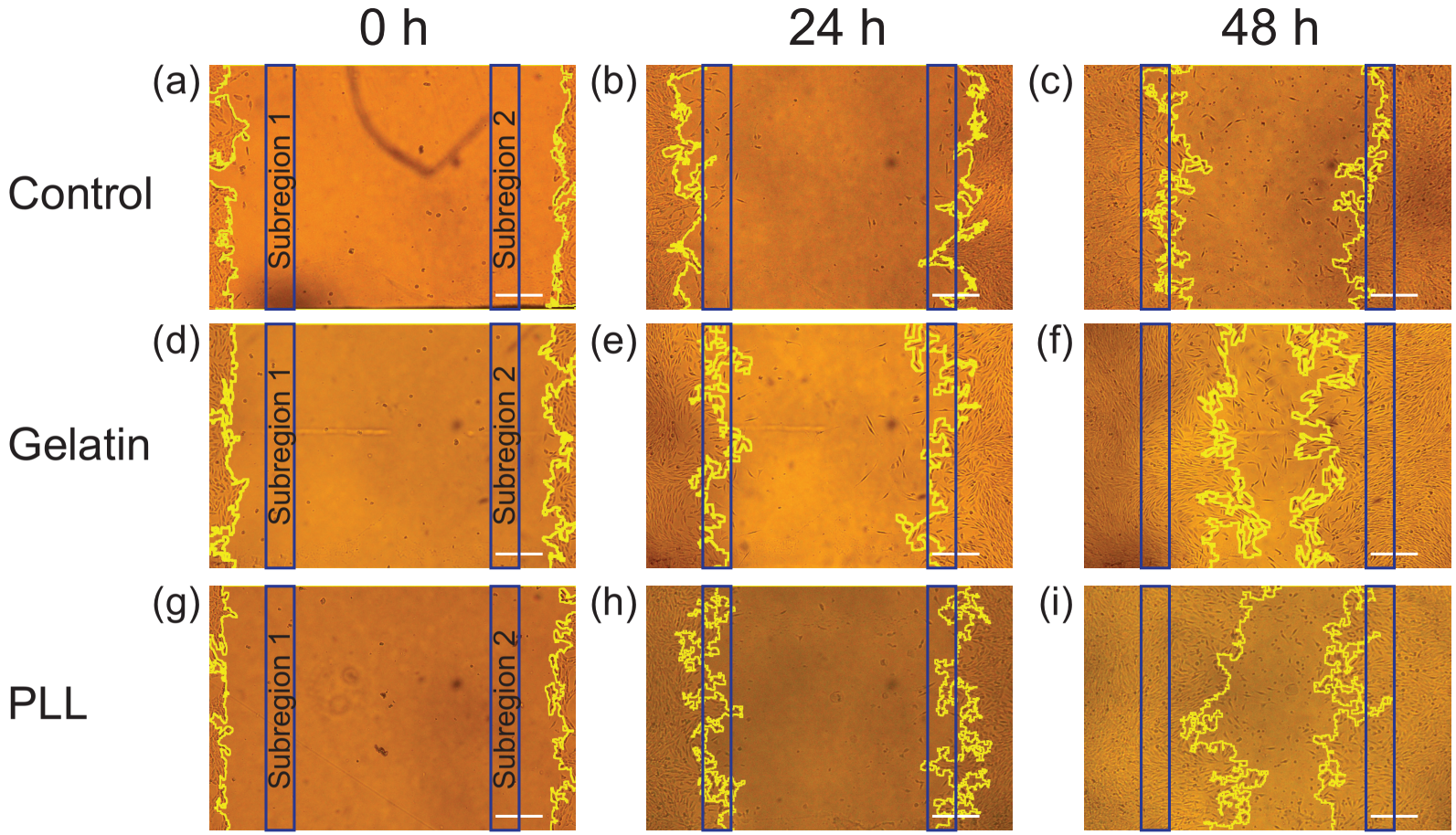

Fig. 2. **Experimental images at $t = 0$, 24, and 48 h from stopper assays.** (a)–(c) Experimental images of the control experiment. (d)–(f) Experimental images of the gelatin–coated experiments. (g)–(i) Experimental images of the PLL–coated experiments. All images show the experimental field-of-view in the upper half of the experimental well, indicated by the black arrow in Figure 1(f)–(g). The yellow line indicates detected edge of the wound area produced by ImageJ. The rectangle highlighted in blue indicates the area in which cell numbers are counted over time. The scale bar corresponds to 500 μm.

2.3 Mathematical model: the Fisher–Kolmogorov model

The Fisher-Kolmogorov model is a reaction–diffusion equation given by

$$\frac{\partial \bar{C}(x,y,t)}{\partial t} = \overbrace{D\nabla^2 \bar{C}(x,y,t)}^{\text{linear diffusion}} + \overbrace{\lambda \bar{C}(x,y,t)\left(1 - \frac{\bar{C}(x,y,t)}{K}\right)}^{\text{logistic growth}}, \tag{1}$$

on $0 \leq x \leq X$, $0 \leq y \leq Y$, where X and Y are the horizontal length and vertical height of the experimental field-of-view, respectively (see Figure 3(a)–(b)) and $t \geq 0$ is time. In this model $\bar{C}(x,y,t) \geq 0$ [cells/μm^2] is the cell density, $D \geq 0$ [μm^2/h] is the cell diffusivity, $\lambda \geq 0$ [/h] is the cell proliferation rate, and $K > 0$ [cells/μm^2] is the carrying capacity density. Since all cells, both inside and outside of the experimental field-of-view, are uniformly seeded we define our simulation domain to be a horizontal extension of the experimental field-of-view, by doubling the length to avoid boundary effects. Therefore, we solve Equation (1) on $-X/2 \leq x \leq 3X/2$, and $0 \leq y \leq Y$. Zero net flux boundary conditions are applied along the four boundaries (Jin et al. 2016).

Previously, Simpson (2009) showed that a depth-averaging method can be used to simplify two-dimensional reaction-diffusion models into one-dimensional reaction-diffusion models by averaging $\bar{C}(x,y,t)$ in the vertical direction,

$$C(x,t) = \frac{1}{Y}\int_0^Y \bar{C}(x,y,t)\ \mathrm{d}y, \tag{2}$$

where $C(x,t)$ [cells/μm^2] is the one-dimensional vertically averaged cell density. To simplify Equation (1) we integrate both sides of the reaction–diffusion equation with respect to y, and then divide both sides by Y to obtain

$$\frac{\partial C}{\partial t} = D\frac{\partial^2 C}{\partial x^2} + \frac{D}{Y}\left(\left.\frac{\partial C}{\partial y}\right|_Y - \left.\frac{\partial C}{\partial y}\right|_0\right) + \lambda C\left(1 - \frac{C}{K}\right). \tag{3}$$

We note that the second and third terms on the right side of Equation (3) vanish since $\partial C/\partial y = 0$ along the boundaries where $y = 0$ and $y = Y$. Therefore, Equation (3) reduces to

$$\frac{\partial C}{\partial t} = D\frac{\partial^2 C}{\partial x^2} + \lambda C\left(1 - \frac{C}{K}\right). \tag{4}$$

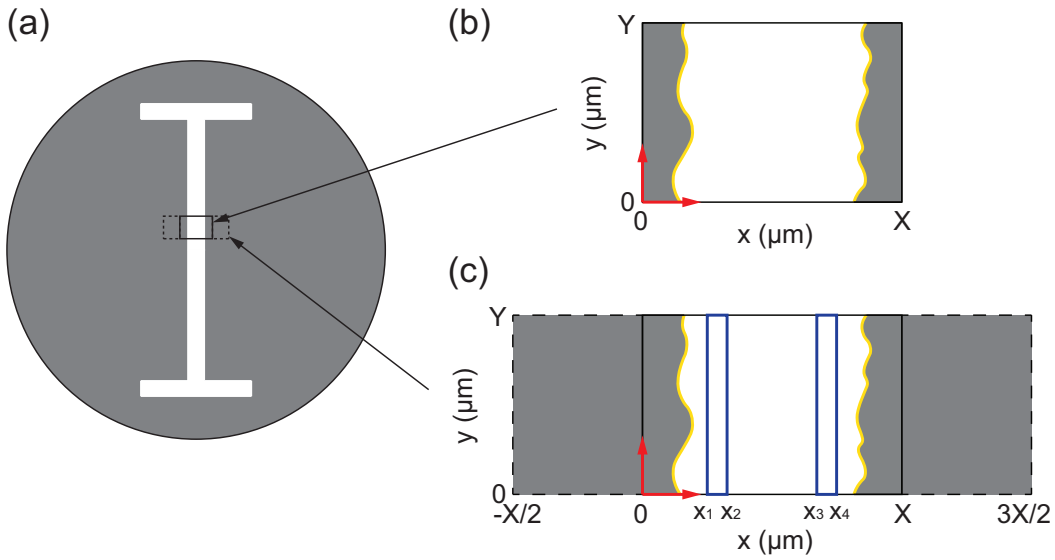

Fig. 3. **Schematics showing the entire experimental well, the experimental field-of-view, and the simulation domain.** (a) Entire experimental well. The white area shows the initial wound made by the stopper. The grey area shows the region where cells are uniformly seeded. (b) Experimental field-of-view, where $X = 1960$ μm, $Y = 1288$ μm and the origin and coordinate system is shown in red. The yellow curve shows the wound edges. (c) Simulation domain. The inner rectangular region (solid lines) shows the actual experimental field-of-view. The outer rectangular region (dashed lines) shows the extended simulation domain. The blue rectangular subregions show the areas where cell numbers are counted.

It is worth noting that simplifying a two–dimensional reaction–diffusion model into a vertically averaged one–dimensional model can introduce an error. However, this error vanishes when the initial condition is uniform in the vertical direction (Simpson, 2009). Since the stopper assays do not involve any cell density gradients in the vertical direction, there is no error associated with averaging the two–dimensional reaction–diffusion equation into the simpler one–dimensional reaction–diffusion equation.

2.3.1 *Estimating wound width using the Fisher-Kolmogorov model*

One feature of the Fisher-Kolmogorov model is that its solutions do not have compact support (McCue et al., 2019). A level set $\epsilon \in [0, 1]$, needs to be nominated to represent edges of the wound. The choice of ϵ also affects the computation of wound width, $\mathcal{W}(t)$. To estimate $\mathcal{W}(t)$ from the numerical solution of Equation (4), we calculate the x coordinates, x_{l} and x_{r}, at left and right side of the wound, respectively, which satisfies $C(x_{\mathrm{l}}, t) = C(x_{\mathrm{r}}, t) = \epsilon$. With this data the wound width is given by $\mathcal{W}(t) = x_{\mathrm{r}} - x_{\mathrm{l}}$, provided $x_{\mathrm{r}} > x_{\mathrm{l}}$. Otherwise $\mathcal{W}(t) = 0$. When we calibrate the mathematical model to a particular experimental replicate we use a superscript to denote the particular replicate. For example, $\mathcal{W}^{(r)}(t)$ denotes the wound width predicted by the model for experimental replicate r.

2.3.2 *Estimating the number of cells using the Fisher-Kolmogorov model*

The number of cells within Subregion 1 and Subregion 2 can be calculated by integrating the cell density, $C(x, t)$, over the two subregions, giving

$$\mathcal{N}_1(t) = Y \int_{x_1}^{x_2} C(x, t)\, \mathrm{d}x, \qquad \text{and} \qquad \mathcal{N}_2(t) = Y \int_{x_3}^{x_4} C(x, t)\, \mathrm{d}x, \tag{5}$$

where $C(x, t)$ is the cell density obtained by solving Equation (4) numerically. To simplify the data that we use to compare the experiments to the model predictions we average $\mathcal{N}_1(t)$ and $\mathcal{N}_2(t)$,

$$\mathcal{N}(t) = \frac{\mathcal{N}_1(t) + \mathcal{N}_2(t)}{2}. \tag{6}$$

Again, when we calibrate the mathematical model to a particular experimental replicate we use a superscript to denote the particular replicate. For example, $\mathcal{N}^{(r)}(t)$ denotes the number of cells predicted by the model for experimental replicate r.

3 Results and discussion

3.1 Experimental estimates of $\widetilde{W}(t)$ and $\widetilde{N}(t)$

Using the methods described in Section 2.2, we obtain estimates of $\widetilde{W}(t)$ and $\widetilde{N}(t)$ for the gelatin, PLL, and control experiments (Figure 4(a)–(b)). This average data indicates that $\widetilde{W}(t)$ decreases fastest for the gelatin–coated experiments and slowest for the control experiments. We also see similar trends in terms of $\widetilde{N}(t)$ data. In all cases we see that $\widetilde{N}(0) \approx 0$ and that the experiments with gelatin coating lead to $\widetilde{N}(t)$ increasing fastest while the control experiments lead to the slowest increase in $\widetilde{N}(t)$.

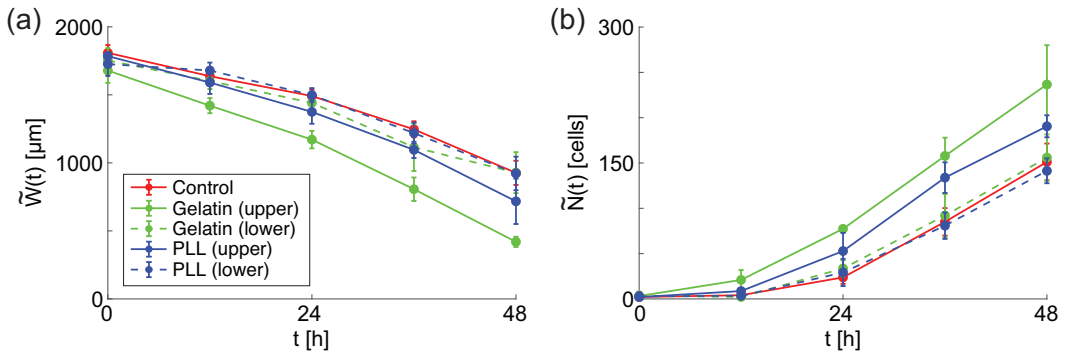

Fig. 4. **Time evolution of $\widetilde{W}(t)$ and $\widetilde{N}(t)$** (a) Time evolution of $\widetilde{W}(t)$ for the control, gelatin, and PLL experiments. (b) Time evolution of $\widetilde{N}(t)$ for the control, gelatin, and PLL experiments. Data points correspond to the sample mean and the error bars indicate the sample standard deviation.

In summary, our experimental data shows that different coatings lead to different estimates of $\widetilde{W}(t)$ and $\widetilde{N}(t)$. For example, both coatings lead to $\widetilde{N}(t)$ that increases faster than $\widetilde{N}(t)$ for the control experiments. One naive way to interpret this difference is that the coatings stimulate cell proliferation. However, as we will now show, when we carefully interpret the experimental data using the Fisher–Kolmogorov model it suggests that the coatings stimulate cell migration but not cell proliferation.

To match the number of cells data with the solution of the Fisher-Kolmogorov

model, we integrate both sides of Equation (4) with respect to x across the two subregions to give

$$\frac{\mathrm{d}\mathcal{N}_1}{\mathrm{d}t} = \overbrace{-D\frac{\partial C}{\partial x}\bigg|_{x_1}}^{\substack{\text{flux into the left boundary} \\ \text{of Subregion 1}}} + \overbrace{D\frac{\partial C}{\partial x}\bigg|_{x_2}}^{\substack{\text{flux out of the right boundary} \\ \text{of Subregion 1}}} + \overbrace{\lambda\int_{x_1}^{x_2} C\left(1-\frac{C}{K}\right)\,\mathrm{d}x}^{\substack{\text{population change in Subregion 1} \\ \text{due to cell proliferation}}}, \tag{7}$$

$$\frac{\mathrm{d}\mathcal{N}_2}{\mathrm{d}t} = \overbrace{-D\frac{\partial C}{\partial x}\bigg|_{x_3}}^{\substack{\text{flux into the left boundary} \\ \text{of Subregion 2}}} + \overbrace{D\frac{\partial C}{\partial x}\bigg|_{x_4}}^{\substack{\text{flux out of the right boundary} \\ \text{of Subregion 2}}} + \overbrace{\lambda\int_{x_3}^{x_4} C\left(1-\frac{C}{K}\right)\,\mathrm{d}x}^{\substack{\text{population change in Subregion 2} \\ \text{due to cell proliferation}}}. \tag{8}$$

Equations (7)–(8) show that the rate of change of cell numbers in particular subregions is driven by the net flux of cells across the boundaries of the subregion and the effect of the proliferation term within the subregion. Therefore, the increase in $\mathcal{N}(t)$ is driven both by the migration term and the proliferation term in Equation (4). Similarly the decrease in the width of the wound, $\mathcal{W}(t)$, is also driven by combined cell migration and cell proliferation terms in Equation (4). Without carefully interpreting the experimental data using a mathematical model it is very difficult to separate the effects of cell migration from cell proliferation in these kinds of experiments. We will now calibrate the solution of Equation (4) to match the data for individual replicates, but first we will estimate the carrying capacity density and the initial condition separately.

3.2 Specifying the carrying capacity density and the initial condition

We directly measure the carrying capacity density, K, from the experimental images (Supplementary Material). Direct counting of maximum cell densities at the final time point of the experiments gives $K = 2.43 \pm 0.36 \times 10^{-3}$ cells/μm^2. We find that our estimates of K are very similar for the control, PLL and gelatin experiments so we have pooled all these estimates together (Supplementary Material). Since we find that K does not vary significantly

between different replicates or between different coating conditions, we treat K as a constant.

Unlike the carrying capacity density, we find that there are some differences in the details of the initial conditions in the various experimental replicates. Therefore we specify a different initial condition for each replicate by counting cells away from the initial wound region. The initial condition for each replicate is given by

$$C^{(r)}(x,0) = \begin{cases} \mathcal{C}_0^{(r)}, & x \leq \frac{X - W^{(r)}(0)}{2}, \\ 0 & \frac{X - W^{(r)}(0)}{2} < x < \frac{X + W^{(r)}(0)}{2}, \\ \mathcal{C}_0^{(r)}, & x \geq \frac{X + W^{(r)}(0)}{2}, \end{cases} \tag{9}$$

where $W^{(r)}(0)$ is the initial width of experimental replicate r and $\mathcal{C}_0^{(r)}$ is the cell density away from the initial wound region in experimental replicate r. We extract these quantities from each experimental replicate and report them in the Supplementary Material document.

3.3 Calibrating the cell diffusivity and the cell proliferation rate

In this section we calibrate the solution of Equation (4) to match both the $W^{(r)}(t)$ and $N^{(r)}(t)$ data from each individual experimental replicate. We solve Equation (4) using a finite difference method, with our measurements of $C^{(r)}(x,0)$ and K (Supplementary Material). In Figure 5(a)–(c) we plot the solution of Equation (4), $C(x,t)$ at $t = 0, 12, 24, 36$, and 48 h, for replicate 2 for the control, gelatin and PLL experiments, respectively. Using these solutions we compute $\mathcal{W}(t)$ and $\mathcal{N}(t)$, and with these estimates we calibrate D, λ and ϵ using MATLAB's *lsqcurvefit* algorithm (MathWorks, 2017) to provide the best match to the experimental data (Supplementary Material). We use a least–squares measure of the discrepancy between the data and the model

solution, given by

$$E^{(r)}(D,\lambda,\epsilon) = \sum_{j=1}^{5}\left[\frac{\mathcal{W}(t_j) - W^{(r)}(t_j)}{W^{(r)}_{\max}}\right]^2 + \left[\frac{\mathcal{N}(t_j) - N^{(r)}(t_j)}{N^{(r)}_{\max}}\right]^2, \qquad (10)$$

where j is an index that indicates the number of time points, and $W^{(r)}_{\max}$ and $N^{(r)}_{\max}$ are the largest wound width and number of cells in experimental replicate r, respectively. For the gelatin and PLL experiments, we have $r = 1, 2$, and 3, while for the regrouped control experiment, $r = 1, 2, \ldots, 9$. Calibrating the solution of the model to data from each experimental replicate gives us several estimates of $\bar{D}^{(r)}$, $\bar{\lambda}^{(r)}$ and $\bar{\epsilon}^{(r)}$ (Supplementary Material). Since these estimates do not vary too much we average them across the replicates to give $\bar{D}$, $\bar{\lambda}$, $\bar{\epsilon}$, together with estimates of the uncertainty in Table 1.

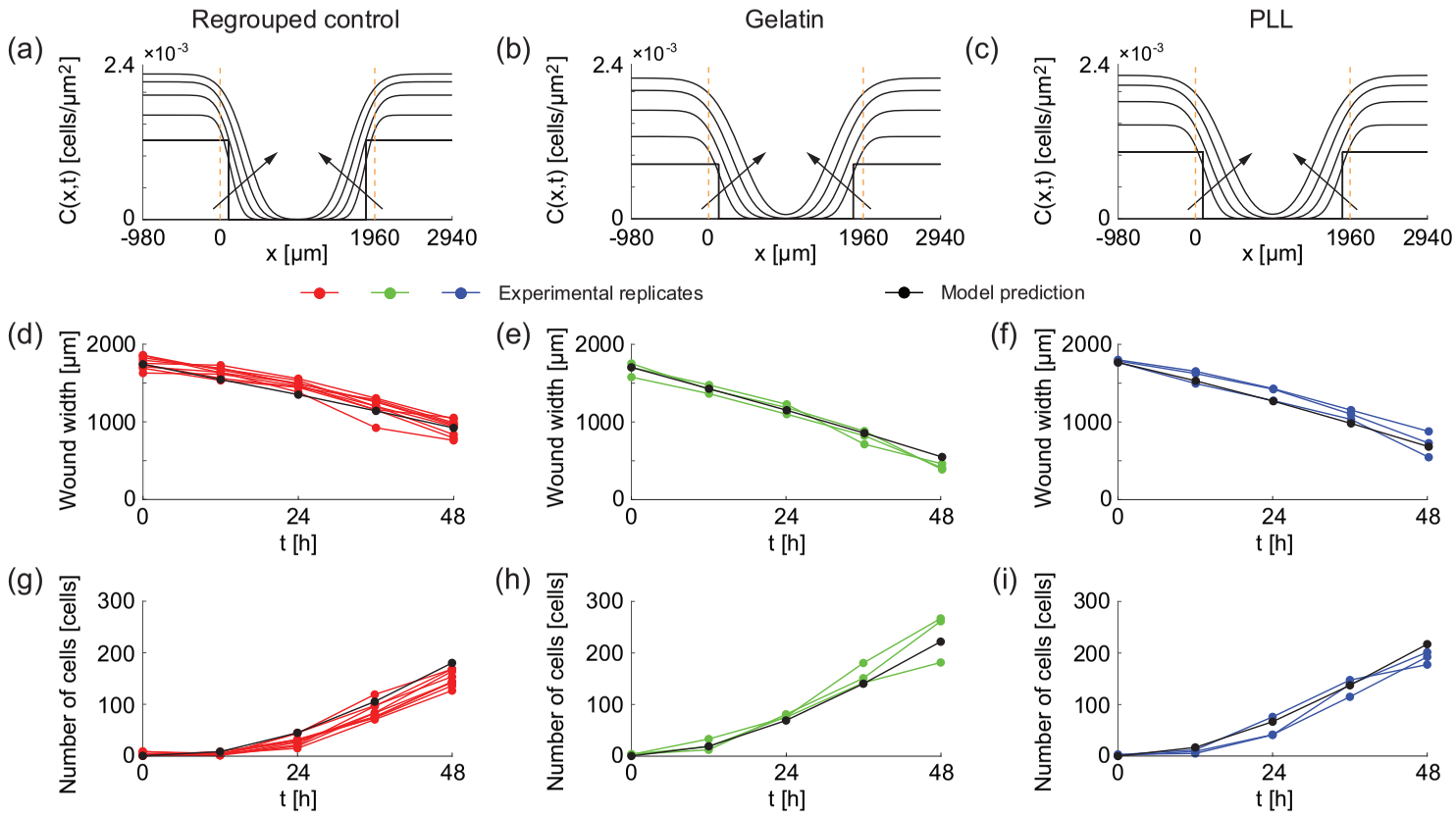

Fig. 5. **Comparing calibrated solutions of the Fisher-Kolmogrov model and the experimental data.** (a)–(c) Numerical solutions of Equation (4) at $t = 0, 12, 24, 36$, and 48 h, using $\bar{D}$ and $\bar{\lambda}$, with $C^{(2)}(x, 0)$ and $W^{(2)}(0)$ for experimental replicate 2. The arrow indicates the direction of increasing t. The orange dashed vertical lines indicate the experimental field-of-view. (d)–(f) Time evolution of $\mathcal{W}^{(2)}(t)$ from the calibrated solution of Equation (4) superimposed on the data, $W^{(r)}(t)$, $r = 1, \ldots, R$. (g)–(i) Time evolution of $\mathcal{N}(t)$ from the calibrated solution of Equation (4) superimposed on the data, $N^{(r)}(t)$, $r = 1, \ldots, R$. In (d), (g), $R = 9$. In (e), (f), (h), (i), $R = 3$.

Table 1

Estimates of $\bar{D}$, $\bar{\lambda}$, and $\bar{\epsilon}$ from individual experimental data. All parameter estimates are given to two significant figures.

	$\bar{D}$ (μm^2/h)	$\bar{\lambda}$ (/h)	$\bar{\epsilon}$ (% of K)
Control	600 ± 240	0.057 ± 0.0061	17 ± 2.7
Gelatin	1000 ± 140	0.061 ± 0.019	12 ± 2.9
PLL	1000 ± 390	0.059 ± 0.012	17 ± 2.9

Our estimates of $\bar{D}$, $\bar{\lambda}$ and $\bar{\epsilon}$ are within previously reported ranges for fibroblast cells (Jin et al., 2018b; Simpson et al., 2013; Tremel et al., 2009). Comparing estimates of $\bar{D}$ and $\bar{\lambda}$ indicates that both the gelatin and PLL coatings stimulate cell migration by about 70% compared to the regrouped control experiment. However, the proliferation rate $\bar{\lambda}$ does not vary over the three groups. Therefore, we find that gelatin and PLL coatings lead to increased cell motility, whereas neither coatings have any significant impact on cell proliferation.

Furthermore, our estimates of $\bar{D}$ for the gelatin and PLL coatings are the same, suggesting that the impact of gelatin and PLL coatings on cell motility is similar. Results in Figure 5(d)–(i) show $\mathcal{W}^{(2)}(t)$ and $\mathcal{N}^{(2)}(t)$ obtained using the calibrated parameter values, superimposed with the $W^{(r)}(t)$ and $N^{(r)}(t)$ data for the individual experimental replicates. These results confirm that the calibrated solution of the Fisher–Kolmogorov model is consistent with the experimental data.

4 Conclusions

In vitro experimental approaches often study the effect of surface coatings simply by comparing images of experiments with coatings to control experiments without coatings. While such comparisons provide information about the net effect of the coating, the simple observations do not provide any insight into

how the coating affects the cell-level mechanisms. For example, observing that a particular coating increases the rate of wound closure provides no insight into whether the increase in the rate of wound closure is driven by an increase in cell motility, an increase in cell proliferation, or a combined increase in cell migration and cell proliferation.

In this work we take a different, more quantitative approach to assess the impact of different coatings on *in vitro* wound–healing experiments. We are motivated to take this approach because we aim to understand how different coatings affect different mechanisms. We consider three types of experiments including control assays without any coating as well as assays with gelatin and PLL coatings. In each experiment we extract two types of data: first we consider the wound width as a function of time; second we consider the number of cells contained within particular subregions as a function of time. By carefully calibrating the solution of the Fisher–Kolmogorov model to match this data we obtain estimates of the cell diffusivity, D, and the cell proliferation rate, λ, and we find that our estimates of these parameters do not very too much between different identically prepared experimental replicates. Comparing estimates of D and λ between the control, gelatin, and PLL experiments indicates that these two coatings increase cell migration by approximately 70% whereas the coatings have negligible impact on the cell proliferation.

Overall, our results suggest that care ought to be taken when interpreting the experimental data. For example, simply counting the number of cells within particular subregions of the experiment shows that the number of cells increases more dramatically in the experiments with PLL and gelatin coatings. Our modelling suggests that this increase in cell number is driven by the coatings stimulating cell migration without influencing the rate of cell proliferation. This conclusion might not be obvious without interpreting our experimental data with a mechanistic mathematical model.

Acknowledgments. We are supported by the Australian Research Council (DP170100474) and the Taiwan Ministry of Science and Technology (MOST 106-2313-B-002-

031-MY3, MOST 107-2221-E-030-001-MY2). Wang Jin is supported by a QUT Vice Chancellor's Research Fellowship.

References

[1] Ascione F, Caserta S, Guido S, 2017. The wound healing assay revisited: A transport phenomena approach. Chem Eng Sci. 160, 200–209.

[2] Barrandon Y, Green H, 1987. Cell migration is essential for sustained growth of keratinocyte colonies: the roles of transforming growth factor-α and epidermal growth factor. Cell. 50, 1131-1137.

[3] Fischer S, Uetz-von Allmen E, Waeckerle-Men Y, Groettrup M, Merkle HP, Gander B, 2007. The preservation of phenotype and functionality of dendritic cells upon phagocytosis of polyelectrolyte-coated PLGA microparticles. Biomaterials. 28, 994-1004.

[4] Fisher RA, 1937. The wave of advance of advantageous genes. Ann Eugen. 7, 353–369.

[5] Hay ED (Ed.), 1991. Cell Biology of Extracellular Matrix. Springer Science & Business Media, New York.

[6] Horiguchi M, Ota M, Rifkin DB, 2012. Matrix control of transforming growth factor-β function. J Biochem. 152, 321-329.

[7] Jin W, Shah ET, Penington CJ, McCue SW, Chopin LK, Simpson MJ, 2016. Reproducibility of scratch assays is affected by the initial degree of confluence: Experiments, modelling and model selection. J Theor Biol. 390, 136–145.

[8] Jin W, Liang X, Brooks A, Futrega K, Liu X, Doran MR, Simpson MJ, Roberts MS, Wang H, 2018a. Modelling of the SDF-1/CXCR4 regulated *in vivo* homing of therapeutic mesenchymal stem/stromal cells in mice. PeerJ. 6, e6072.

[9] Jin W, Lo KY, Chou SE, McCue SW, Simpson MJ, 2018b. The role of initial geometry in experimental models of wound closing. Chem Eng Sci. 179, 221-226.

[10] Johnston ST, Simpson MJ, McElwain DLS, 2014. How much information can be obtained from tracking the position of the leading edge in a scratch assay? J R Soc Interface. 11, 20140325.

[11] Jove M, Spencer JA, Hubbard ME, Holden EC, O'Dea RD, Brook BS, Phillips RM, Smye SW, Loadman PM, Twelves CJ, 2019. Cellular uptake and efflux of palbociclib in vitro in single cell and spheroid models. J Pharmacol Exp Ther. 370, 242-251.

[12] Liang CC, Park AY, Guan JL, 2007. *In vitro* scratch assay: a convenient and inexpensive method for analysis of cell migration *in vitro*. Nat Protoc. 2, 329-333.

[13] Liberio MS, Sadowski MC, Soekmadji C, Davis RA, Nelson CC, 2014. Differential effects of tissue culture coating substrates on prostate cancer cell adherence, morphology and behavior. PLOS ONE. 9, e112122.

[14] Maini PK, McElwain DLS, Leavesley DI, 2004. Travelling waves in a wound healing assay. Appl Math Lett. 17, 575-580.

[15] MathWorks. Lsqcurvefit. https://au.mathworks.com/help/optim/ug/lsqcurvefit.html (Accessed: Nov 2019).

[16] McCarthy JB, Palm SL, Furcht LT, 1983. Migration by haptotaxis of a Schwann cell tumor line to the basement membrane glycoprotein laminin. J Cell Biol. 97, 772-777.

[17] McCue SW, Jin W, Moroney TJ, Lo KY, Chou SE, Simpson MJ, 2019. Hole-closing model reveals exponents for nonlinear degenerate diffusivity functions in cell biology. Physica D. 398, 130-140.

[18] McIntosh LC, Muckersie L, Forrester JV, 1988. Retinal capillary endothelial cells prefer different substrates for growth and migration. Tissue Cell. 20, 193-209.

[19] Nardini JT, Chapnick DA, Liu X, Bortz DM, 2016. Modeling keratinocyte wound healing dynamics: Cell-cell adhesion promotes sustained collective migration. J Theor Biol. 400, 103-117.

[20] Rangappa N, Romero A, Nelson KD, Eberhart RC, Smith GM, 2000. Laminin-coated poly (L-lactide) filaments induce robust neurite growth while providing directional orientation. J Biomed Mater Res. 51, 625-634.

[21] Schindelin J, Rueden CT, Hiner MC, Eliceiri KW, 2015. The ImageJ ecosystem: An open platform for biomedical image analysis. Mol Reprod Dev. 82, 518-529.

[22] Screen HR, Berk DE, Kadler KE, Ramirez F, Young MF, 2015. Tendon functional extracellular matrix. J Orthop Res. 33, 793-799.

[23] Sengers BG, Please CP, Oreffo RO, 2007. Experimental characterization and computational modelling of two-dimensional cell spreading for skeletal regeneration. J R Soc Interface. 4, 1107-1117.

[24] Sheardown H, Cheng YL, 1996. Mechanisms of corneal epithelial wound healing. Chem Eng Sci. 51, 4517-4529.

[25] Sherratt JA, Murray JD, 1990. Models of epidermal wound healing. P Roy Soc Lond B Bio. 241, 29-36.

[26] Simpson MJ, 2009. Depth-averaging errors in reactive transport modeling. Water Resour Res. 45, W02505.

[27] Simpson MJ, Treloar KK, Binder BJ, Haridas P, Manton KJ, Leavesley DI, McElwain DLS, Baker RE, 2013. Quantifying the roles of cell motility and cell proliferation in a circular barrier assay. J R Soc Interface. 10, 20130007.

[28] Tam A, Green JE, Balasuriya S, Tek EL, Gardner JM, Sundstrom JF, Jiranek V, Binder BJ, 2019. A thin-film extensional flow model for biofilm expansion by sliding motility. P R Soc A. 475, 20190175.

[29] Treloar KK, Simpson MJ, 2013. Sensitivity of edge detection methods for quantifying cell migration assays. PLOS ONE. 8, e67389.

[30] Tremel A, Cai A, Tirtaatmadja N, Hughes BD, Stevens GW, Landman KA, O'Connor AJ, 2009. Cell migration and proliferation during monolayer formation and wound healing. Chem Eng Sci. 64, 247–253.

[31] Vedula SR, Ravasio A, Lim CT, Ladoux B, 2013. Collective cell migration: a mechanistic perspective. Physiology. 28, 370-379.

[32] Villella VR, Venerando A, Cozza G, Esposito S, Ferrari E, Monzani R, Spinella MC, Oikonomou V, Renga G, Tosco A, Rossin F, Guido S, Silano M, Garaci E, Chao Y, Grimm C, Luciani A, Romani L, Piacentini M, Raia V, Kroemer G, Maiuri L, 2019. A pathogenic role for cystic fibrosis transmembrane conductance regulator in celiac disease. EMBO J. 38, e100101.

Supplementary Material: Quantifying the role of different surface coatings in experimental models of wound healing

Wang Jin [a,*], Kai-Yin Lo [b], Yung-Shin Sun [c], Ya-Han Ting [b], Matthew J Simpson [a],

[a] *School of Mathematical Sciences, Queensland University of Technology (QUT) Brisbane, Queensland 4000, Australia.*

[b] *Department of Agricultural Chemistry, National Taiwan University Taipei 10617, Taiwan.*

[c] *Department of Physics, Fu-Jen Catholic University, Taipei 242, Taiwan.*

---

[*] Corresponding author.
Email address: w1.jin@qut.edu.au (Wang Jin).

Contents

1 Numerical methods for solving the Fisher-Kolmogorov model

The one-dimensional Fisher-Kolmogorov equation is of the form

$$\frac{\partial C}{\partial t} = D\frac{\partial^2 C}{\partial x^2} + \lambda C\left(1 - \frac{C}{K}\right), \tag{S1}$$

on $-980 \leq x \leq 2940$ μm, where D [μm^2/h] is the cell diffusivity, λ [/h] is the cell proliferation rate, and K [cells/μm^2] is the carrying capacity density. To numerically solve Equation (S1), the spatial domain is discretised into M nodes using a central difference approximation with uniform spacing δx. Here we denote C_i as the cell density at a discretised node i, where $i = 1, 2, 3, \ldots, M$. The discretisation for the internal nodes at time t is as follows

$$\frac{\mathrm{d}C_i(t)}{\mathrm{d}t} = \frac{D}{\delta x^2}\Big(C_{i+1}(t) - 2C_i(t) + C_{i-1}(t)\Big) + \lambda C_i(t)\left(1 - \frac{C_i(t)}{K}\right), \tag{S2}$$

for $i = 2, \ldots, M-1$. We apply zero net flux boundary condition at both boundaries, i.e., $C_2 = C_1$ and $C_M = C_{M-1}$. The initial condition is obtained by measuring cell densities from the experimental images at $t = 0$ h, with the average data and data for individual replicates given in Table S5 and Table S16, respectively. The resulting system of nonlinear ordinary differential equations is integrated using a backward Euler method with constant time step δt, which leads to a system of coupled nonlinear algebraic equations linearised and solved using the Thomas algorithm, with the absolute tolerance η (Morton and Mayers, 2005). For all results presented in the main manuscript as well as the supplementary material, we choose $\delta x = 0.5$ μm, $\delta t = 0.1$ h, and $\eta = 1 \times 10^{-5}$ so that our results are grid-independent.

2 Model calibration and additional parameter estimates data

We numerically solve the one-dimensional Fisher-Kolmogorov model (Equation (S1)) using a finite difference method, with $C^{(r)}(x,0)$ and K measured from the experimental images. Using the numerical methods introduced in Section 1, we obtain the density profiles at $t = 0, 12, 24, 36$, and 48 h. We then compute $\mathcal{W}(t)$ and $\mathcal{N}(t)$, and with these estimates we calibrate D and λ for the regrouped control, gelatin, and PLL experiments. We systematically vary ϵ, from $0.01K - 0.25K$, to identify the level set that minimises the least-squares measure of the discrepancy between the data and the model solution, given in Equation (10) in the main manuscript.

To consider the variation in the parameter estimates, we calibrate the solution of Equation (S1) to match the $W^{(r)}(t)$ and $N^{(r)}(t)$ data from each individual replicate. We find that each case appears to have a well-defined minimum, from which we estimate $\bar{D}^{(r)}$, $\bar{\lambda}^{(r)}$, and $\bar{\epsilon}^{(r)}$. We then average them across the replicates to give $\bar{D}$, $\bar{\lambda}$, and $\bar{\epsilon}$, which are listed in Table 1 in the main manuscript. In this supplementary material, we show histograms of the parameter estimates of the cell diffusivity $\bar{D}^{(r)}$ and proliferation rate $\bar{\lambda}^{(r)}$ for individual replicates in Figure S1. The estimated parameter values for individual replicates are listed in Table S1 - Table S3.

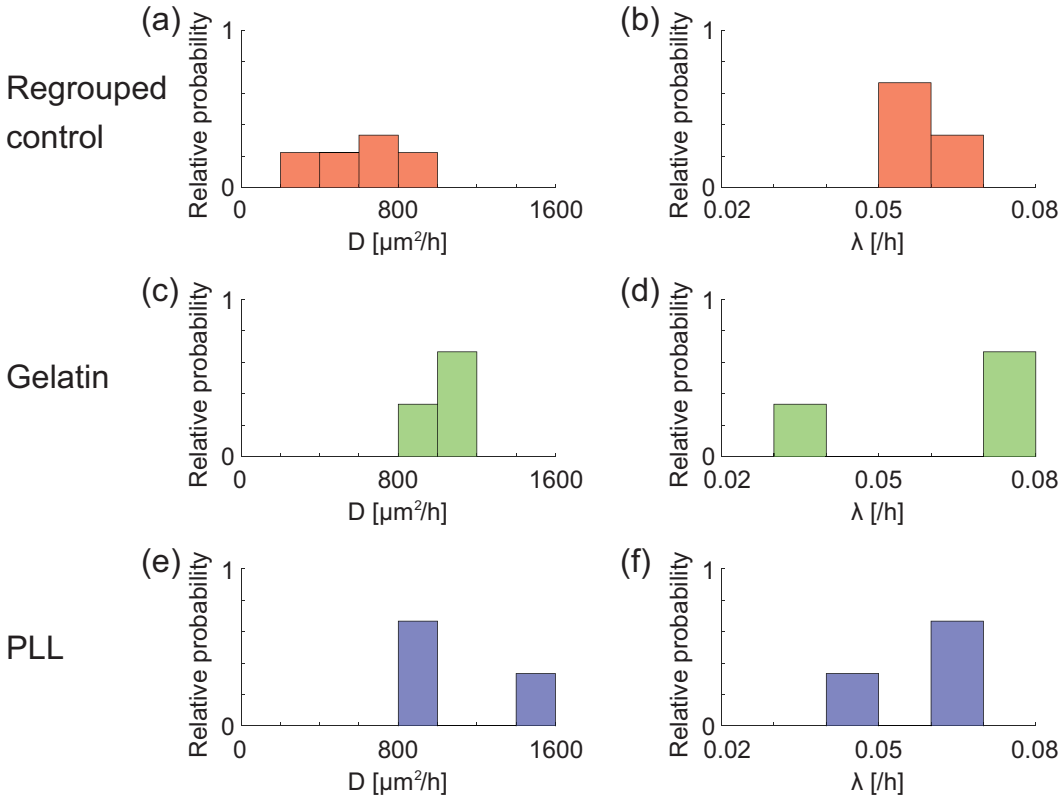

Fig. S1. **Histograms of parameter estimates of the cell diffusivity $\bar{D}^{(r)}$ and proliferation rate $\bar{\lambda}^{(r)}$.** The three rows correspond to the parameter estimates for the regrouped control, gelatin, and PLL experiments, respectively.

Table S1

Estimates of $\bar{D}$ and $\bar{\lambda}$ for individual replicates in the regrouped control experiment. All parameter estimates are given to two significant figures. The red column in each replicate indicates the level set which gives the minimum least-squares measure.

Regrouped control		Level set ϵ (% of K)					
		1	5	10	15	20	25
Replicate 1	$\bar{D}^{(1)}$ [μm^2/h]	220	370	500	610	660	660
	$\bar{\lambda}^{(1)}$ [/h]	0.12	0.088	0.075	0.068	0.066	0.066
	$E^{(1)}$ ($\times 10^{-2}$)	13	5.8	2.7	1.4	1.4	2.5
Replicate 2	$\bar{D}^{(2)}$ [μm^2/h]	180	290	380	460	490	500
	$\bar{\lambda}^{(2)}$ [/h]	0.099	0.072	0.060	0.054	0.051	0.051
	$E^{(2)}$ ($\times 10^{-2}$)	12	4.9	1.8	0.53	0.43	1.2
Replicate 3	$\bar{D}^{(3)}$ [μm^2/h]	260	440	590	720	760	710
	$\bar{\lambda}^{(3)}$ [/h]	0.11	0.080	0.068	0.061	0.060	0.063
	$E^{(3)}$ ($\times 10^{-2}$)	14	6.0	2.3	0.85	1.1	2.7
Replicate 4	$\bar{D}^{(4)}$ [μm^2/h]	210	350	490	620	680	660
	$\bar{\lambda}^{(4)}$ [/h]	0.13	0.094	0.079	0.070	0.067	0.069
	$E^{(4)}$ ($\times 10^{-2}$)	12	5.4	2.1	0.71	0.56	1.5
Replicate 5	$\bar{D}^{(5)}$ [μm^2/h]	160	250	320	370	390	380
	$\bar{\lambda}^{(5)}$ [/h]	0.087	0.066	0.056	0.051	0.049	0.051
	$E^{(5)}$ ($\times 10^{-2}$)	9.6	3.6	1.1	0.36	0.63	1.6
Replicate 6	$\bar{D}^{(6)}$ [μm^2/h]	280	470	660	800	910	890
	$\bar{\lambda}^{(6)}$ [/h]	0.086	0.066	0.057	0.053	0.051	0.053
	$E^{(6)}$ ($\times 10^{-2}$)	14	6.5	3.5	2.9	4.1	7.1
Replicate 7	$\bar{D}^{(7)}$ [μm^2/h]	160	280	360	430	450	460
	$\bar{\lambda}^{(7)}$ [/h]	0.11	0.077	0.066	0.060	0.058	0.058
	$E^{(7)}$ ($\times 10^{-2}$)	16	7.9	4.0	2.2	1.6	1.9
Replicate 8	$\bar{D}^{(8)}$ [μm^2/h]	110	160	190	210	200	210
	$\bar{\lambda}^{(8)}$ [/h]	0.092	0.070	0.061	0.057	0.059	0.059
	$E^{(8)}$ ($\times 10^{-2}$)	8.2	4.1	2.6	2.2	2.3	2.8
Replicate 9	$\bar{D}^{(9)}$ [μm^2/h]	300	500	770	1000	1200	1100
	$\bar{\lambda}^{(9)}$ [/h]	0.093	0.072	0.059	0.052	0.050	0.052
	$E^{(9)}$ ($\times 10^{-2}$)	18	8.4	3.4	1.1	1.2	3.7

Table S2

Estimates of $\bar{D}$ and $\bar{\lambda}$ for individual replicates in the gelatin experiment. All parameter estimates are given to two significant figures. The red column in each replicate indicates the level set which gives the minimum least-squares measure.

Gelatin		Level set ϵ (% of K)				
		1	5	10	15	20
Replicate 1	$\bar{D}^{(1)}$ [μm^2/h]	360	590	830	1100	1400
	$\bar{\lambda}^{(1)}$ [/h]	0.11	0.088	0.078	0.071	0.066
	$E^{(1)}$ ($\times 10^{-2}$)	6.8	2.4	0.89	0.62	1.3
Replicate 2	$\bar{D}^{(2)}$ [μm^2/h]	340	560	830	1100	1500
	$\bar{\lambda}^{(2)}$ [/h]	0.10	0.083	0.073	0.067	0.061
	$E^{(2)}$ ($\times 10^{-2}$)	6.0	2.4	1.3	1.3	2.4
Replicate 3	$\bar{D}^{(3)}$ [μm^2/h]	360	650	1000	1500	2400
	$\bar{\lambda}^{(3)}$ [/h]	0.059	0.046	0.039	0.034	0.031
	$E^{(3)}$ ($\times 10^{-2}$)	8.3	3.2	2.1	3.1	5.8

Table S3

Estimates of $\bar{D}$ and $\bar{\lambda}$ for individual replicates in the PLL experiment. All parameter estimates are given to two significant figures. The red column in each replicate indicates the level set which gives the minimum least-squares measure.

PLL		Level set ϵ (% of K)					
		1	5	10	15	20	25
Replicate 1	$\bar{D}^{(1)}$ [μm^2/h]	240	380	520	660	800	880
	$\bar{\lambda}^{(1)}$ [/h]	0.12	0.093	0.080	0.072	0.066	0.064
	$E^{(1)}$ ($\times 10^{-2}$)	18	9.2	4.8	2.5	1.3	1.3
Replicate 2	$\bar{D}^{(2)}$ [μm^2/h]	450	760	1100	1500	2000	2200
	$\bar{\lambda}^{(2)}$ [/h]	0.078	0.061	0.052	0.046	0.042	0.043
	$E^{(2)}$ ($\times 10^{-2}$)	22	11	5.2	2.9	3.1	6
Replicate 3	$\bar{D}^{(3)}$ [μm^2/h]	250	440	630	840	1000	1100
	$\bar{\lambda}^{(3)}$ [/h]	0.11	0.086	0.074	0.066	0.061	0.062
	$E^{(3)}$ ($\times 10^{-2}$)	12	4.9	1.8	0.43	0.66	2.6

3 Experimental data describing the carrying capacity density, the initial cell density, and the initial wound width

In this section, we discuss the measure of carrying capacity density, K, and initial cell density, $\mathcal{C}_0^{(r)}$, for the experimental replicates. Our experimental results suggest that regions far behind the edges of the wound are fully occupied by cells after 48 h. Therefore, we directly count the number of cells at $t = 48$ h in the four identical 300 μm $\times$ 150 μm rectangular boxes, located 50 μm away from the edges of the experimental field-of-view (Figure S2). By averaging the number of cells over the four boxes in each replicate and then further averaging across the individual replicates, we obtain estimates of K listed in Table S4.

To estimate $\mathcal{C}_0^{(r)}$ we count and average the number of cells in the same four identically-sized rectangular boxes for replicate r at $t = 0$ h. In Table S5 we show the estimates of $\widetilde{\mathcal{C}}_0$ for the control, gelatin, and PLL experiments, obtained by averaging $\mathcal{C}_0^{(r)}$ across the individual replicates in each experiment.

In addition, in Table S6 we show the data of the average initial wound width, $\widetilde{W}(0)$, estimated using the wound edge detection method (Jin et al. 2018).

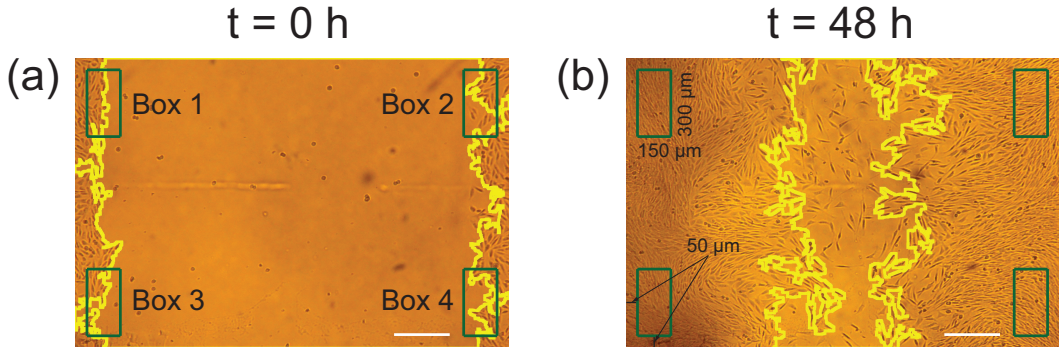

Fig. S2. **Examples of experimental images at $t = 0$ and 48 h.** The green rectangular boxes indicate regions where cell number is counted. The yellow lines indicate the wound edges. The scale bar corresponds to 500 μm.

Table S4

Estimates of K obtained by measuring and averaging cell numbers in the four identically-sized boxes in experimental images at $t = 48$ h. All estimates are rounded to two decimal places.

K [cells/μm^2]		Average from replicates	Standard deviation
Control		2.46×10^{-3}	3.88×10^{-4}
Gelatin	Upper	2.48×10^{-3}	8.94×10^{-5}
	Lower	2.34×10^{-3}	6.58×10^{-5}
PLL	Upper	2.41×10^{-3}	8.14×10^{-5}
	Lower	2.45×10^{-3}	7.59×10^{-5}
Average from experiments		2.43×10^{-3}	3.60×10^{-4}

Table S5

Estimates of $\widetilde{\mathcal{C}}_0$ obtained by measuring and averaging cell numbers in the four identically-sized boxes in experimental images at $t = 0$ h. All estimates are rounded to two decimal places.

$\widetilde{\mathcal{C}}_0$ [cells/μm^2]		Average from replicates	Standard deviation
Control		1.00×10^{-3}	4.15×10^{-4}
Gelatin	Upper	9.81×10^{-4}	3.51×10^{-4}
	Lower	1.03×10^{-3}	2.99×10^{-4}
PLL	Upper	9.39×10^{-4}	3.02×10^{-4}
	Lower	1.18×10^{-3}	5.35×10^{-4}
Average from experiments		1.02×10^{-3}	3.91×10^{-4}

Table S6

Estimates of $\widetilde{W}(0)$ measured from experimental images at $t = 0$ h. All estimates are rounded to the nearest integer.

$\widetilde{W}(0)$ [μm]		Average from replicates	Standard deviation
Control		1809	57
Gelatin	Upper	1678	90
	Lower	1753	90
PLL	Upper	1785	17
	Lower	1726	87
Average from experiments		1750	51

4 Experimental data for individual replicates

Table S7 - Table S9 list the data of $W^{(r)}(t)$ and $N^{(r)}(t)$ for the three replicates in the control experiment. Table S10 - Table S12 list the data of $W^{(r)}(t)$ and $N^{(r)}(t)$ for the three replicates in the gelatin experiment. Table S13 - Table S15 list the data of $W^{(r)}(t)$ and $N^{(r)}(t)$ for the three replicates in the PLL experiment. Table S16 shows the data of $\mathcal{C}_0^{(r)}$ and $K^{(r)}$ measured from individual replicates.

Table S7

Experimental data of $W^{(1)}(t)$ and $N^{(1)}(t)$ for replicate 1 in the control experiment.

Control 1	$W^{(1)}(t)$ [μm]		$N^{(1)}(t)$ [cells]			
t [h]	Upper	Lower	Upper		Lower	
			$N_1^{(1)}(t)$	$N_2^{(1)}(t)$	$N_1^{(1)}(t)$	$N_2^{(1)}(t)$
0	1838	1816	5	3	5	4
12	1686	1680	2	1	3	7
24	1567	1498	12	24	15	33
36	1201	1195	104	62	103	116
48	830	841	164	155	217	137

Table S8

Experimental data of $W^{(2)}(t)$ and $N^{(2)}(t)$ for replicate 2 in the control experiment.

Control 2	$W^{(2)}(t)$ [μm]		$N^{(2)}(t)$ [cells]			
t [h]	Upper	Lower	Upper		Lower	
			$N_1^{(2)}(t)$	$N_2^{(2)}(t)$	$N_1^{(2)}(t)$	$N_2^{(2)}(t)$
0	1745	1737	0	0	2	3
12	1589	1534	9	7	7	9
24	1467	1427	23	35	21	47
36	1279	1290	76	63	76	89
48	996	983	113	153	120	185

Table S9

Experimental data of $W^{(3)}(t)$ and $N^{(3)}(t)$ for replicate 3 in the control experiment.

Control 3	$W^{(3)}(t)$ [μm]		$N^{(3)}(t)$ [cells]			
t [h]	Upper	Lower	Upper		Lower	
			$N_1^{(3)}(t)$	$N_2^{(3)}(t)$	$N_1^{(3)}(t)$	$N_2^{(3)}(t)$
0	1882	1835	4	0	0	0
12	1695	1639	0	1	3	0
24	1504	1485	20	9	14	32
36	1325	1186	22	120	129	61
48	1036	873	132	112	178	148

Table S10

Experimental data of $W^{(1)}(t)$ and $N^{(1)}(t)$ for replicate 1 in the gelatin experiment.

Gelatin 1	$W^{(1)}(t)$ [μm]		$N^{(1)}(t)$ [cells]			
t [h]	Upper	Lower	Upper		Lower	
			$N_1^{(1)}(t)$	$N_2^{(1)}(t)$	$N_1^{(1)}(t)$	$N_2^{(1)}(t)$
0	1753	1856	6	1	13	4
12	1421	1632	23	13	2	0
24	1185	1496	80	72	30	22
36	883	1264	179	182	73	94
48	388	971	270	264	181	147

Table S11

Experimental data of $W^{(2)}(t)$ and $N^{(2)}(t)$ for replicate 2 in the gelatin experiment.

Gelatin 2	$W^{(2)}(t)$ [μm]		$N^{(2)}(t)$ [cells]			
t [h]	Upper	Lower	Upper		Lower	
			$N_1^{(2)}(t)$	$N_2^{(2)}(t)$	$N_1^{(2)}(t)$	$N_2^{(2)}(t)$
0	1704	1711	6	0	1	3
12	1476	1639	10	14	0	3
24	1227	1383	103	59	52	35
36	713	923	151	151	80	158
48	461	761	255	268	156	180

Table S12

Experimental data of $W^{(3)}(t)$ and $N^{(3)}(t)$ for replicate 3 in the gelatin experiment.

Gelatin 3	$W^{(3)}(t)$ [μm]		$N^{(3)}(t)$ [cells]			
t [h]	Upper	Lower	Upper		Lower	
			$N_1^{(3)}(t)$	$N_2^{(3)}(t)$	$N_1^{(3)}(t)$	$N_2^{(3)}(t)$
0	1578	1691	4	2	0	0
12	1365	1534	38	28	1	7
24	1101	1444	68	82	13	50
36	823	1157	151	133	53	94
48	409	1052	174	189	160	112

Table S13

Experimental data of $W^{(1)}(t)$ and $N^{(1)}(t)$ for replicate 1 in the PLL experiment.

PLL 1	$W^{(1)}(t)$ [μm]		$N^{(1)}(t)$ [cells]			
t [h]	Upper	Lower	Upper		Lower	
			$N_1^{(1)}(t)$	$N_2^{(1)}(t)$	$N_1^{(1)}(t)$	$N_2^{(1)}(t)$
0	1800	1753	6	0	9	7
12	1653	1729	7	3	9	0
24	1429	1556	52	30	9	20
36	1153	1304	113	165	57	84
48	879	1035	190	213	163	90

Table S14

Experimental data of $W^{(2)}(t)$ and $N^{(2)}(t)$ for replicate 2 in the PLL experiment.

PLL 2	$W^{(2)}(t)$ [μm]		$N^{(2)}(t)$ [cells]			
t [h]	Upper	Lower	Upper		Lower	
			$N_1^{(2)}(t)$	$N_2^{(2)}(t)$	$N_1^{(2)}(t)$	$N_2^{(2)}(t)$
0	1767	1629	3	2	0	0
12	1495	1615	9	15	7	3
24	1274	1461	91	61	32	25
36	1034	1200	155	140	98	51
48	546	941	198	157	153	135

Table S15

Experimental data of $W^{(3)}(t)$ and $N^{(3)}(t)$ for replicate 3 in the PLL experiment.

PLL 3	$W^{(3)}(t)$ [μm]		$N^{(3)}(t)$ [cells]			
t [h]	Upper	Lower	Upper		Lower	
			$N_1^{(3)}(t)$	$N_2^{(3)}(t)$	$N_1^{(3)}(t)$	$N_2^{(3)}(t)$
0	1786	1796	0	1	0	1
12	1624	1693	17	1	1	1
24	1421	1478	42	41	28	61
36	1101	1153	129	101	113	82
48	727	791	150	235	154	153

Table S16

Experimental data of $\mathcal{C}_0^{(r)}$ and K for individual replicates in the three groups. All the data are given to two decimal places.

t [h]	$\mathcal{C}_0^{(r)}$ [$\times 10^{-3}$ cells/μm^2]								$K^{(r)}$ [$\times 10^{-3}$ cells/μm^2]							
	Upper				Lower				Upper				Lower			
	Box 1	Box 2	Box 3	Box 4	Box 1	Box 2	Box 3	Box 4	Box 1	Box 2	Box 3	Box 4	Box 1	Box 2	Box 3	Box 4
Control 1	1.47	1.10	0.73	0.30	0.97	1.10	0.90	0.93	2.09	2.18	2.31	2.38	1.98	1.60	3.00	2.73
Control 2	1.50	1.03	1.70	1.10	1.53	0.43	1.23	1.43	2.40	2.04	2.20	2.18	2.38	2.47	2.33	2.29
Control 3	0.43	1.57	0.40	1.20	1.10	0.83	0.73	0.37	3.51	2.16	2.44	2.53	2.89	2.73	2.76	2.40
Gelatin 1	1.47	0.83	0.77	0.97	0.73	0.70	1.00	1.03	2.76	2.58	2.53	2.76	2.58	2.60	2.38	2.31
Gelatin 2	1.33	0.83	0.63	0.63	0.87	1.13	0.80	0.80	3.18	2.38	2.96	3.04	2.00	2.31	2.20	2.60
Gelatin 3	1.70	1.10	0.87	0.63	1.47	1.70	1.10	1.07	1.82	1.64	2.47	1.64	2.42	2.09	2.60	2.04
PLL 1	1.10	0.93	1.47	0.60	0.80	1.03	1.17	0.63	2.38	2.27	2.49	2.36	2.62	2.44	2.71	1.84
PLL 2	1.43	0.83	1.07	0.87	2.07	1.87	1.93	1.47	2.07	2.07	2.84	1.98	2.09	2.07	2.16	2.11
PLL 3	1.03	0.60	0.53	0.80	1.07	0.80	0.73	0.53	2.60	2.82	1.89	3.20	2.80	2.71	2.42	1.84

References

[1] Jin W, Lo KY, Chou SE, McCue SW, Simpson MJ, 2018b. The role of initial geometry in experimental models of wound closing. Chem Eng Sci. 179, 221-226.

[2] Morton KW, Mayers DF, 2005. Numerical Solution of Partial Differential Equations. Cambridge University Press, Cambridge.